

Linking Uranus' temperature profile to wind–induced magnetic fields

Deniz Soyuer,[★] and Ravit Helled

Center for Theoretical Astrophysics and Cosmology, Institute for Computational Science, University of Zurich, Winterthurerstrasse 190, CH-8057 Zurich, Switzerland

Accepted 2021 August 3. Received 2021 August 3; in original form 2021 June 10.

arXiv:2108.01604v3 [astro-ph.EP] 7 Aug 2021

ABSTRACT

The low luminosity of Uranus is still a puzzling phenomenon and has key implications for the thermal and compositional gradients within the planet. Recent studies have shown that planetary volatiles become ionically conducting under conditions that are present in the ice giants. Rapidly growing electrical conductivity with increasing depth would couple zonal flows to the background magnetic field in the planets, inducing poloidal and toroidal field perturbations $\mathbf{B}^\omega = \mathbf{B}_P^\omega + \mathbf{B}_T^\omega$ via the ω –effect. Toroidal perturbations \mathbf{B}_T^ω are expected to diffuse downwards and produce poloidal fields \mathbf{B}_P^α through turbulent convection via the α –effect, comparable in strength to those of the ω –effect; \mathbf{B}_P^ω . To estimate the strength of poloidal field perturbations for various Uranus models in the literature, we generate wind decay profiles based on Ohmic dissipation constraints assuming an ionically conducting H₂–He–H₂O interior. Due to the higher metallicities in outer regions of hot Uranus models, zonal winds need to decay to $\sim 0.1\%$ of their surface values in the outer 1% of Uranus to admit decay solutions in the Ohmic framework. Our estimates suggest that colder Uranus models could potentially have poloidal field perturbations that reach up to $\mathcal{O}(0.1)$ of the background magnetic field in the most extreme case. The possible existence of poloidal field perturbations spatially correlated with Uranus' zonal flows could be used to constrain Uranus' interior structure, and presents a further case for the *in situ* exploration of Uranus.

Key words: methods: data analysis – planets and satellites: composition – planets and satellites: individual: Uranus – planets and satellites: interiors – planets and satellites: magnetic fields

1 INTRODUCTION

The solar system's giant planets provide us with an exceptional opportunity for studying the physics of high–pressure, rotating systems with density and compositional variations. Among them, Jupiter and Saturn have been relatively well-studied compared to Uranus and Neptune, which remain the least explored solar system planets to this day. The scientific potential of space missions to Uranus and Neptune is currently being thoroughly assessed by the planetary science community (see e.g. Hofstadter et al. 2019; Helled & Fortney 2020; Dahl et al. 2020; Fletcher et al. 2020a,b; Beddingfield et al. 2020; Moore et al. 2020; Soyuer et al. 2021), and various mission concepts have already being discussed (e.g. Jarmak et al. 2020; Cohen et al. 2020; Cartwright et al. 2020; Simon et al. 2020). The under-exploration of Uranus and Neptune is unfortunate, as these planets exhibit highly multipolar and nonaxisymmetric magnetic fields (Connerney et al. 1987, 1991; Holme & Bloxham 1996), are compositionally more diverse than the gas giants (Helled et al. 2011; Nettelmann et al. 2013), and have a significant contrast in their thermal flux. More specifically, Neptune's energy balance (i.e. the ratio of emitted thermal energy to absorbed solar energy) is 1.5–1.75 times that of gas giants, whereas Uranus is almost in equilibrium with the solar flux (Pearl et al. 1990; Pearl & Conrath 1991).

The last two decades have seen dramatic improvements in mod-

elling dynamos of solar system giants (Stanley & Bloxham 2004, 2006; Soderlund et al. 2013; Dietrich & Jones 2018; Wicht et al. 2019), but our understanding of planetary magnetic fields is still very limited. One of the challenges in modelling planetary dynamos is linked to the fact that the magnetic fields are measured external to the planets, whereas the field itself is generated deeper inside the planet. This inverse source problem makes it difficult to find a unique solution to the dynamo region that generates most of the observed external magnetic fields. This is especially true for the peculiar magnetic fields of ice giants (Soderlund & Stanley 2020), due to the relative lack of data for modelling the magnetic fields (Holme & Bloxham 1996), the compositions (Helled et al. 2011; Nettelmann et al. 2013), and the heat transfer mechanisms inside the planets (Podolak et al. 2019; Vazan & Helled 2020). Understanding the observed surface magnetic field of Uranus and Neptune does not only involve modelling the dynamo generation region, but also the shallow region quasi-dynamo action, which couples the zonal winds to the background magnetic field. Investigations of this coupling have been conducted for the gas giants (Cao & Stevenson 2017; Galanti & Kaspi 2021), where it was found that poloidal magnetic field perturbations that are spatially correlated with the zonal flows were possible (with the strength of 0.01–1 per cent of the background field), and that the zonal wind–magnetic field interaction in the semiconducting region of gas giants plays a key role in zonal flow decay.

We estimate the strength of the shallow layer coupling of the magnetic field to the zonal winds by using the electrical conductiv-

[★] E-mail: deniz.soyuer@uzh.ch

ity prescription for H₂–He–H₂O mixtures provided in [Soyer et al. \(2020\)](#). Inspired by [Cao & Stevenson \(2017\)](#), we look for poloidal field perturbations to the background magnetic field induced by this interaction, via a simplified α – ω mechanism. By compiling sets of zonal wind decay profiles obeying Ohmic dissipation constraints, we estimate the magnitude of poloidal field perturbations for various Uranus models in the literature. Naturally, our simple estimate is not expected to capture the complete physical picture. Nevertheless, the goal of this short paper is to draw attention to this mechanism, and show that a mission to Uranus can significantly improve our understanding of its dynamics, magnetic field and composition.

2 URANUS MODELS

2.1 Interior structure models

We consider five different Uranus density/pressure profiles with nine associated temperature profiles taken from [Helled et al. \(2011\)](#); [Nettelmann et al. \(2013\)](#); [Podolak et al. \(2019\)](#); [Vazan & Helled \(2020\)](#) summarized in Table 1, and explained in detail in [Soyer et al. \(2020\)](#). These models cover a wide range of thermodynamic parameters and also employ different heat transfer mechanisms (convection, double diffusive convection, conduction) and were constructed with various methods and constraints. Namely; U1a is a 3-layer adiabatic profile by [Nettelmann et al. \(2013\)](#), U1b and U1c are the modified double diffusive temperature profiles to U1a by [Podolak et al. \(2019\)](#). U2 is again a 3-layer adiabatic profile by [Nettelmann et al. \(2013\)](#), with a modified rotation period obtained by [Helled et al. \(2010\)](#). U3 and U4 are non-adiabatic models by [Vazan & Helled \(2020\)](#), evolved using various primordial composition distributions and initial energy budgets, to fit present day Uranus models. U5a, U5b and U5c are empirical density profiles by [Helled et al. \(2011\)](#) with various glued temperature profiles by [Podolak et al. \(2019\)](#), described in Table 1. The top panels in Figure 1 show the density, pressure, and temperature profiles of the models for the outer 20% of the planet.

For the purpose of this work we assume the region we are interested in Uranus is composed of a H₂–He–H₂O mixture given by

$$\frac{1}{\rho} = \frac{X}{\rho_{\text{H}_2}} + \frac{Y}{\rho_{\text{He}}} + \frac{Z}{\rho_{\text{H}_2\text{O}}}, \quad (1)$$

with a protosolar ratio of $X/Y = 0.745/0.255$. For hydrogen and helium we adopt the equation of state (EOS) developed by [Chabrier et al. \(2019\)](#) and for water that of [Shah et al. \(2021\)](#). The different EOSs are combined using the above isothermal-isobaric ideal volume law, which is a good approximation under the range of conditions explored in the current work for hydrogen–helium ([Chabrier et al. 2019](#)), for water–hydrogen ([Soubiran & Militzer 2015](#)) and for ternary mixtures ([Soubiran & Militzer 2016](#)). Figure 1 (d) shows the inferred metallicities from this prescription.

2.2 Electrical conductivities

Estimating the ionic conductivity of any H₂–He–[liquid ice] mixture is difficult, let alone generalizing the calculation to various mixture parameters. Arguably, the most notable measurement of electrical conductivity of a mixture resembling the interiors of Uranus and Neptune has been carried out by [Nellis et al. \(1988\)](#). In [Nellis et al. \(1988\)](#), the electrical conductivity of a "synthetic Uranus" mixture composed of water, ammonia and isopropanol (C₃H₈O) has been measured up to 0.75 Mbar (corresponding to 5000 K in their model). The experiment shows that the electrical conductivity of this mixture is similar to that of pure water, measured by [Hamann & Linton](#)

(1966); [Mitchell & Nellis \(1982\)](#) for roughly the same regime. Lately, laser-driven shock-compression experiments have verified the super-sonic conduction of water ice ([Millot et al. 2018](#)), and ammonia ([Ravasio et al. 2021](#)) under planetary conditions.

In [Soyer et al. \(2020\)](#) we have developed a model for estimating the ionic conductivity of H₂–He–H₂O mixtures under planetary conditions. This model makes use of the fluctuation-dissipation theorem, where the autocorrelation of microscopic currents are linked to the electric conductivity of ions in a mixture, taking into account the diffusion, electrical charge and number density of various H and O species. We apply this prescription to various H₂–He–H₂O mixtures that fit to Uranus structure models using the EOSs mentioned above. For a detailed description of the ionic conductivity prescription we refer the reader to [Soyer et al. \(2020\)](#).

Figure 1 (e) shows the radial electrical conductivity profiles calculated for the Uranus structure models. Due to the considerable difference between interior structure models there is a significant variation in electrical conductivity values (reaching up to three orders of magnitude at 0.85R_U). Hotter models reach higher conductivity levels mainly due to higher metallicities (i.e. higher water concentration) and due to the increase in the fraction of ionized H and O species with temperature.

2.3 Zonal flow decay

Uranus exhibits fast zonal winds on the surface with speeds reaching up to roughly 200 m s^{−1} with respect to its rotation. The surface wind profile has a retrograde motion around the equator and prograde motion at higher latitudes, fit by

$$v_{\varphi,U}(r = R_U, \theta) = 170 \times (0.6 \sin \theta + \sin 3\theta) \text{ ms}^{-1}, \quad (2)$$

where θ is the co-latitude ([Hammel et al. 2001](#)).

It is commonly assumed that the surface winds continue downward into the planet, along cylinders parallel to the planetary rotation axis. There is evidence from gravity data that winds are expected to attenuate with depth in Uranus and Neptune ([Kaspi et al. 2013](#)). Indeed, deep-seated strong winds would violate energy and entropy constraints throughout the planet's interiors due to excess Ohmic dissipation caused by their interaction with the background magnetic field ([Soyer et al. 2020](#)). Relatively shallow winds also seem to be the case in the gas giants, where estimates based on Juno and Cassini gravity data ([Kaspi et al. 2018, 2020](#); [Galanti & Kaspi 2021](#)) have similar implications to those based on Ohmic dissipation constraints ([Liu et al. 2008](#); [Wicht et al. 2019](#)).

We define a general behaviour for an azimuthally symmetric zonal wind profile $U_{\varphi}(r, \theta, n_i)$ with a radial decay profile $\mathcal{B}(r, n_i)$, where n_i are any parameters describing the decay:

$$U_{\varphi}(r, \theta, n_i) = v_{\varphi}(\mathcal{A}(r, \theta)) \times \mathcal{B}(r, n_i). \quad (3)$$

Here, $\mathcal{A}(r, \theta)$ describes the relationship of any point (r, θ) inside the planet to the surface wind profile $v_{\varphi}(r = R_U, \theta)$. In the case of winds retaining their surface profile along lines parallel to the rotation axis, this would be $\mathcal{A}(r, \theta) = \arcsin(r \sin \theta / R_U)$. For zonal wind decay inside the planet, we adopt a simple exponential decay. More sophisticated models for the wind decay such as that in [Galanti & Kaspi \(2021\)](#) have been also considered, and have yielded very similar results to those of the exponential decay. Thus, here we adopt an exponential decay for simplicity with an e-folding depth H :

$$\mathcal{B}(r, H) = \exp((r/R_U - 1)/H). \quad (4)$$

Table 1. List of the interior structure models of Uranus used in this study. Model numbers correspond to various density/pressure profiles. Letters following the model number (e.g. U1a, U1b, U1c) represent different temperature profiles for the same density/pressure profile. The original names of the structure models in their respective papers are shown on the right column.

Density/Pressure Profile	Temperature Profile	Rotation Period	Convective Layers	Original Name
U1a Nettelmann et al. (2013)	Nettelmann et al. (2013)	17.24h	1	U1
U1b Nettelmann et al. (2013)	Podolak et al. (2019)	17.24h	1	U1 Cold Model
U1c Nettelmann et al. (2013)	Podolak et al. (2019)	17.24h	10^6	U1 Hot Model
U2 Nettelmann et al. (2013)	Nettelmann et al. (2013)	16.58h	1	U2
U3 Vazan & Helled (2020)	Vazan & Helled (2020)	17.24h	–	V3
U4 Vazan & Helled (2020)	Vazan & Helled (2020)	17.24h	–	V4
U5a Helled et al. (2011)	Podolak et al. (2019)	17.24h	1	PolyU Cold Model
U5b Helled et al. (2011)	Podolak et al. (2019)	17.24h	10^6	PolyU Hot Model
U5c Helled et al. (2011)	Podolak et al. (2019)	17.24h	10^7	–

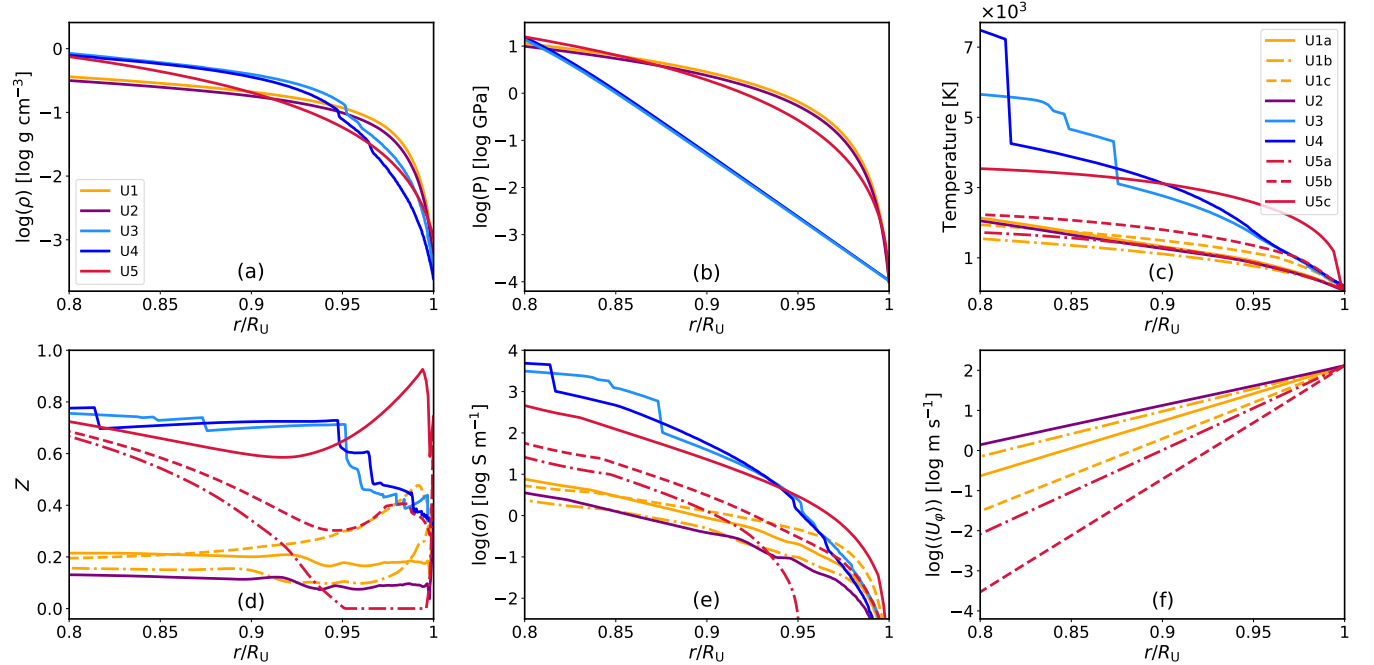


Figure 1. (a): Radial density profiles of various published Uranus structure models (Helled et al. 2011; Nettelmann et al. 2013; Podolak et al. 2019; Vazan & Helled 2020). (b): Radial pressure profiles of the same models. (c): Various radial temperature profiles corresponding to the interior structure profiles by color. Different line styles represent alternative temperature profiles for the same colored density/pressure model. (d): Inferred radial metallicity profiles assuming an ideally mixed H₂–He–H₂O mixture and the aforementioned EOS's. (e): Radial electrical conductivity profiles calculated using the interior structure profiles, using the prescription in Soyuer et al. (2020) for ionically conducting H₂–He–H₂O mixtures. (f): The highest allowed rms zonal flow speeds for each interior structure model, evaluated in the aforementioned parameter range. In hot models U3, U4 and U5c, winds need to decay to ~0.1% of their surface values to admit solutions. Thus, we exclude them from our perturbation analysis and omit them in the last panel.

2.4 Ohmic dissipation

The induced electrical currents due to the interaction of the zonal flows with the magnetic field produce Ohmic dissipation given by

$$P = \int \frac{j^2}{\sigma} dV, \quad (5)$$

where j is the current density given by Ohm's law: $j = \sigma(E + \mathbf{U} \times \mathbf{B})$. The prescription for calculating the current densities are omitted for brevity, but are provided explicitly in Liu (2006); Soyuer et al. (2020).

The current densities can be approximated as

$$j_\theta \approx \frac{\sigma(r)}{r} \left(\partial_\theta \int_r^R (\mathbf{U}_\varphi \times \mathbf{B}_P^0)_r dr' + r(\mathbf{U}_\varphi \times \mathbf{B}_P^0)_\theta \right), \quad (6a)$$

$$j_\varphi \approx \frac{\sigma(r)}{r} \partial_\varphi \int_r^R (\mathbf{U}_\varphi \times \mathbf{B}_P^0)_r dr', \quad (6b)$$

where the radial currents j_r are suppressed due to the rapidly varying radial electrical conductivity.

Using equation (5), we compile sets of zonal wind decay profiles $\{U_\varphi \mid P(U_\varphi) < P_{\lim}\}$ for the various Uranus models, where we explore the parameter space $H \geq 0.01$ with the requirement that the Ohmic dissipation P remains smaller than an Ohmic dissipation limit P_{\lim} . The total Ohmic dissipation can be constrained by the energy

or the entropy budget throughout the planetary interior (Hewitt et al. 1975; Wicht et al. 2019). We choose the latter as our limit for two reasons; (i) it does not require the adiabatic cooling to cancel out dissipative heating at each radius, and (ii) it provides a looser constraint compared to the former, allowing us to probe a larger range of flow decay profiles. We consider the Ohmic dissipation generated above $r = 0.8R_U$ and use the entropy limit

$$P(U_\varphi)|_{0.8R_U} \stackrel{!}{\leq} P_{\text{lim}} = \left(\frac{T(r = 0.8R_U)}{T_0} - 1 \right) L, \quad (7)$$

with L being Uranus' surface luminosity and T_0 is the temperature at the boundary of the convective envelope, which we set as the 1 bar temperature, given by the structure models. Since the Ohmic dissipation per volume associated with the zonal flows is proportional to $p \propto j^2/\sigma \propto U_\varphi^2 \sigma$, the contribution to the total built-up Ohmic dissipation starts to diminish after some depth. This occurs due to saturating electrical conductivity and fast zonal flow decay. Therefore, considering the Ohmic dissipation generated above $r = 0.8R_U$ is an adequate approximation. It also has the added benefit of avoiding the uncertainties in Ohmic dissipation generation arising in the dynamo generation region, and allowing us to probe a greater range of decay profiles due to a less stringent constraint.

It is convenient to describe the zonal wind strength as a function of depth via the rms zonal wind velocity, given by:

$$\langle U_\varphi \rangle(r) = \left(\frac{1}{2} \int_0^\pi U_\varphi(r, \theta)^2 \sin \theta d\theta \right)^{1/2}. \quad (8)$$

The last panel in Figure 1 shows the rms zonal flows that have the highest allowed speeds at $0.8R_U$ for Uranus structure models, satisfying the entropy limit. It is clear from the figure that colder models permit zonal flows that can reach up to 1 m s^{-1} at $r = 0.80R_U$. For hot models U3, U4 and U5c the zonal winds need to decay to $\sim 0.1\%$ of their surface values to admit solutions in the Ohmic dissipation framework. Note that the plotted zonal wind velocities are the fastest speeds allowed in the Ohmic dissipation framework. Namely, existence of such wind decay profiles would imply that the entropy at $r > 0.8R_U$ is solely generated by the induced currents due to zonal winds.

The inferred magnetic Reynolds number for these zonal flows are shown in the left panel of Figure 2, defined as

$$R_m(U_\varphi) = \mu_0 \sigma \langle U_\varphi \rangle H_\sigma, \quad (9)$$

with σ being the electrical conductivity and $H_\sigma = \sigma/\partial_r \sigma$ is the associated scale height. $R_m(U_\varphi)$ essentially describes the zonal wind–background magnetic field coupling in this region.

3 MAGNETIC FIELD PERTURBATIONS

Planetary magnetic fields \mathbf{B} are generally decomposed into their poloidal \mathbf{B}_P and toroidal \mathbf{B}_T components (Backus 1986), such that

$$\mathbf{B} = \mathbf{B}_P + \mathbf{B}_T, \text{ with } \mathbf{r} \cdot (\nabla \times \mathbf{B}_P) = 0 \text{ and } \mathbf{r} \cdot \mathbf{B}_T = 0. \quad (10)$$

Uranus' magnetic field is modelled so that the toroidal component vanishes $\mathbf{B}_T = 0$ external to the planet due to the absence of currents. At the surface ($r = R_U, \theta, \phi$), we separate the magnetic field into two parts $\mathbf{B}_{\text{surf.}} = \mathbf{B}_P^0 + \mathbf{B}'_P$, where we define \mathbf{B}_P^0 as the background poloidal field (Holme & Bloxham 1996) and \mathbf{B}'_P as the poloidal perturbation to \mathbf{B}_P^0 . We take the surface field as the background field $\mathbf{B}_P^0 \sim \mathbf{B}_{\text{surf.}}$ and extrapolate it downwards. This approximation will not affect the final estimate for the perturbation, since $\mathbf{B}'_P \ll \mathbf{B}_P^0$.

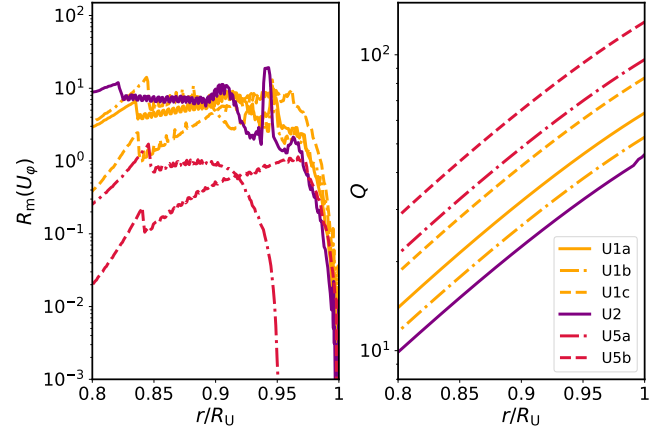


Figure 2. Left panel: The magnetic Reynolds number $R_m(U_\varphi)$ associated with the extreme zonal flows shown in Figure 1. Right panel: Ratio Q of toroidal field to poloidal field generation given in equation (13) for wind decay corresponding to those presented in Figure 1. Although the poloidal field generation is up to two orders of magnitude smaller than the toroidal field generation, it could still have a significant contribution to the total detectable poloidal perturbation \mathbf{B}'_P . This is because the toroidal field \mathbf{B}_T^ω will cause a poloidal perturbation with a strength of order $\mathbf{B}_T^\omega R_m(\alpha)$, where $R_m(\alpha)$ is between 10^{-3} and 10^{-2} at $r = 0.8R_U$ for these models.

We model the generation of the perturbation \mathbf{B}'_P following in the footsteps of Cao & Stevenson (2017) with an extra term due to the nonaxisymmetric magnetic field of Uranus:

- (i) With increasing depth, zonal winds couple to the background poloidal field via the ω -effect, which induces a field $\mathbf{B}^\omega = \mathbf{B}_T^\omega + \mathbf{B}'_P$.
- (ii) The poloidal part \mathbf{B}'_P is the first contribution to the detectable field perturbation at the surface \mathbf{B}'_P .
- (iii) The toroidal part \mathbf{B}_T^ω is then expected to diffuse downwards due to the rapidly increasing electrical conductivity. The α -effect acts on the wind induced toroidal field \mathbf{B}_T^ω and generates a poloidal field \mathbf{B}^α , the second contribution to \mathbf{B}'_P .

Hence, the total poloidal perturbation spatially correlated with the zonal flows and detectable at the surface is given by

$$\mathbf{B}'_P = \mathbf{B}_P^\omega + \mathbf{B}^\alpha. \quad (11)$$

In order to estimate the ratio of the toroidal to poloidal contribution of the ω -effect–induced fields, we look at the generative part (subscript g) of the induction equation

$$(\partial_t \mathbf{B}^\omega)_g = \nabla \times (\mathbf{U} \times \mathbf{B}^0) = - \frac{U_\varphi \partial_\varphi B_r^0}{r \sin \theta} \hat{r} - \frac{U_\varphi \partial_\varphi B_\theta^0}{r \sin \theta} \hat{\theta} + \frac{\partial_r (r U_\varphi B_r^0) + \partial_\theta (U_\varphi B_\theta^0)}{r} \hat{\varphi}, \quad (12)$$

and set the ratio as the azimuthal field generation to the sum of the radial and latitudinal field generation:

$$Q := \frac{\mathbf{B}_P^\omega(r)}{\mathbf{B}'_P(r)} \sim \frac{\langle (\partial_t \mathbf{B}^\omega)_g \cdot \hat{\varphi} \rangle}{\langle (\partial_t \mathbf{B}^\omega)_g \cdot \hat{r} \rangle + \langle (\partial_t \mathbf{B}^\omega)_g \cdot \hat{\theta} \rangle}, \quad (13)$$

where $\langle \cdot \rangle$ here denotes spherically averaged rms values, i.e. over θ and φ defined analogously to equation (8):

$$\langle f(\mathbf{r}) \rangle = \langle f \rangle(r) = \frac{1}{2} \left(\int_0^\pi \int_0^{2\pi} f(\mathbf{r})^2 d\varphi \sin \theta d\theta \right)^{1/2}. \quad (14)$$

Figure 2 shows the ratio Q in equation (13) for the various extreme

zonal wind decay profiles given in the bottom center panel of Figure 1. The field generation in the azimuthal direction is up to two orders of magnitude larger than in the poloidal direction.

An important caveat is that the α -effect is not straightforward to model and is the biggest unknown in the prescription. The magnetic Reynolds number associated with the α -effect is given by

$$R_m(\alpha) = \mu_0 \sigma \alpha H_\sigma, \quad (15)$$

where α is the strength of the effect (Cao & Stevenson 2017). To first order, the strength of the perturbations scale as

$$B_P^\omega = B^\omega - B_T^\omega \sim R_m(U_\varphi) B_P^0 - B_T^\omega = \frac{R_m(U_\varphi) B_P^0}{1+Q}, \quad (16)$$

$$B_P^\alpha \sim R_m(\alpha) B_T^\omega = Q R_m(\alpha) B_P^\omega, \quad (17)$$

and the ratio of the perturbation to the background field is then expressed as

$$\frac{B_P^\omega + B_P^\alpha}{B_P^0} \sim (1 + Q R_m(\alpha)) \frac{R_m(U_\varphi)}{1+Q}. \quad (18)$$

Note that, the two magnetic Reynolds numbers are calculated at different depths. $R_m(U_\varphi)$ peaks and then saturates (or decreases steadily for slow zonal flows) in the region we have already explored. The α -effect is more pronounced with increasing conductivity, hence $R_m(\alpha)$ as well. In Cao & Stevenson (2017), α is taken to be a scalar functional proportional to the electrical conductivity and having a strength of 0.1 mm s^{-1} at the depth where $\sigma = 10^3 \text{ S m}^{-1}$, corresponding to 10% of the estimated convective velocity in gas giants at that depth. This is taken to be the base of the semiconducting region in gas giants, i.e., the threshold below which the mean-field induction equation becomes inadequate for describing the behavior of magnetic field generation. Using the same α -effect strength for our estimations, we get poloidal perturbations that can reach up to

$$\frac{B_P^\omega + B_P^\alpha}{B_P^0} = \mathcal{O}(0.1) \quad (19)$$

for the coldest models (which have flatter zonal wind decay). Clearly, this estimate cannot capture the complete physical picture. Indeed, as seen in Cao & Stevenson (2017) for example, the ratio of the calculated toroidal field perturbation to the background magnetic field is one order of magnitude lower than $R_m(U_\varphi)$, when the mean-field equations are solved for an axisymmetric field. Nevertheless, the detection of zonal wind-induced magnetic field perturbations is possible even for values that are orders of magnitude smaller than this value. Even the sensitivity of the magnetometer of *Voyager II* was of the order of 0.1 nT (roughly a millionth of the surface field strength in ice giants) (Holme & Bloxham 1996).

4 DISCUSSION AND CONCLUSION

In this short paper, we have investigated the zonal flow–background magnetic field interaction in Uranus. Our findings suggest that:

(i) Due to their high temperatures in outer regions of hot Uranus models, the winds need to decay to $\sim 0.1\%$ of their surface values in the outer 1% of Uranus to admit decay solutions.

(ii) Colder models of Uranus do admit flatter decay solutions and can have wind speeds up to 1 m s^{-1} at $r = 0.80 R_U$ in the extreme.

(iii) Assuming the same α -effect strength present at the bottom of the semiconducting region of gas giants, poloidal field perturbations generated by the zonal wind–magnetic field–convection interaction in ice giants can reach up to $\mathcal{O}(0.1)$ of the background field.

For the last point we repeat the three important caveats that should be considered. First, the scaling given in equation (18) is a simplification of the interaction between the zonal wind and magnetic field, and the poloidal perturbation to background field ratio estimated here is roughly an upper limit. Second, the uncertainty in the α -effect coupling is not trivial. However, via the constraints that will be put on the heat transfer mechanisms after a mission, a better estimate for the α -effect can be constructed. Most importantly, the zonal wind velocities probed here represent the *fastest speeds* allowed in the Ohmic dissipation framework. Such wind decay profiles mean that the entropy at $r > 0.8 R_U$ is solely generated by the zonal winds–magnetic field interaction, which is most probably not the case.

It should be noted that our estimates all use the ionic conductivity estimates from Soyuer et al. (2020), and assume that Uranus is composed of a mixture of $\text{H}_2\text{-He-H}_2\text{O}$ in the region of interest. Clearly, the composition of Uranus is more complex and includes other constituents. However, volatiles like water, ammonia and also similar mixtures are expected to become electrically conducting (Mitchell & Nellis 1982; Nellis et al. 1988; Millot et al. 2018; Ravasio et al. 2021), and to have similar conductivities with our estimates. Nevertheless, electrical conductivities of volatile mixtures under planetary conditions requires further research.

Given that region where the perturbations are generated is shallow, high order harmonics might be pronounced at the planetary surface. However, in order to get a more complete understanding of the zonal wind–magnetic field interaction in general, the mean-field induction equations for the toroidal and poloidal field perturbations in the rapidly increasing conductivity region should be modelled and numerically solved. The nonaxisymmetry of the surface magnetic fields, the uncertainty of convective velocities, and the possible existence of an inner/outer envelope boundary within ice giants makes this topic challenging and future measurements as well as theoretical calculations are required. It is clear that there are still many key open questions regarding the nature of Uranus (and Neptune). We suggest that a space mission to Uranus would significantly improve our understanding of its internal structure and composition, the origin of its dynamo, its dynamics and their interplay, and will allow us to test and further develop the ideas presented in this work.

ACKNOWLEDGEMENTS

We thank the anonymous referee for valuable comments and suggestions. We thank Hao Cao, David Stevenson, François Soubiran, Yohai Kaspi and Eli Galanti for their feedback on the manuscript. We acknowledge support from SNSF grant 200020_188460 and the National Centre for Competence in Research ‘PlanetS’ supported by SNSF.

DATA AVAILABILITY

Models in this work are those used in Soyuer et al. (2020) and will be shared on request to the corresponding author(s) with permission.

REFERENCES

- Backus G., 1986, *Reviews of Geophysics*, **24**, 75
- Beddingfield C., et al., 2020, arXiv e-prints, p. arXiv:2007.11063
- Cao H., Stevenson D. J., 2017, *Icarus*, **296**, 59
- Cartwright R. J., et al., 2020, arXiv e-prints, p. arXiv:2007.07284
- Chabrier G., Mazeved S., Soubiran F., 2019, *ApJ*, **872**, 51

Cohen I. J., et al., 2020, in Lunar and Planetary Science Conference. Lunar and Planetary Science Conference. p. 1428

Connerney J. E. P., Acuna M. H., Ness N. F., 1987, *J. Geophys. Res.*, **92**, 15329

Connerney J. E. P., Acuna M. H., Ness N. F., 1991, *J. Geophys. Res.*, **96**, 19023

Dahl E. K., et al., 2020, arXiv e-prints, p. arXiv:2010.08617

Dietrich W., Jones C. A., 2018, *Icarus*, **305**, 15

Fletcher L. N., et al., 2020a, *Planet. Space Sci.*, **191**, 105030

Fletcher L. N., Simon A. A., Hofstadter M. D., Arridge C. S., Cohen I. J., Masters A., Mandt K., Coustenis A., 2020b, *Philosophical Transactions of the Royal Society of London Series A*, **378**, 20190473

Galanti E., Kaspi Y., 2021, *MNRAS*, **501**, 2352

Hamann S. D., Linton M., 1966, *Trans. Faraday Soc.*, **62**, 2234

Hammel H., Rages K., Lockwood G., Karkoschka E., de Pater I., 2001, *Icarus*, **153**, 229

Helled R., Fortney J. J., 2020, *Philosophical Transactions of the Royal Society of London Series A*, **378**, 00474

Helled R., Anderson J. D., Schubert G., 2010, *Icarus*, **210**, 446

Helled R., Anderson J. D., Podolak M., Schubert G., 2011, *ApJ*, **726**, 15

Hewitt J. M., Mckenzie D. P., Weiss N. O., 1975, *Journal of Fluid Mechanics*, **68**, 721–738

Hofstadter M., et al., 2019, *Planet. Space Sci.*, **177**, 104680

Holme R., Bloxham J., 1996, *J. Geophys. Res.*, **101**, 2177

Jarmak S., et al., 2020, *Acta Astronautica*, **170**, 6

Kaspi Y., Showman A. P., Hubbard W. B., Aharonson O., Helled R., 2013, *Nature*, **497**, 344

Kaspi Y., et al., 2018, *Nature*, **555**, 223

Kaspi Y., Galanti E., Showman A. P., Stevenson D. J., Guillot T., Iess L., Bolton S. J., 2020, *Space Sci. Rev.*, **216**, 84

Liu J., 2006, PhD thesis, California Institute of Technology, <https://search.proquest.com/docview/305356554?accountid=14796>

Liu J., Goldreich P. M., Stevenson D. J., 2008, *Icarus*, **196**, 653

Millot M., et al., 2018, *Nature Physics*, **14**, 297

Mitchell A. C., Nellis W. J., 1982, *J. Chem. Phys.*, **76**, 6273

Moore J., et al., 2020, Exploration Strategy for the Outer Planets 2023-2032: Goals and Priorities (arXiv:2003.11182)

Nellis W. J., Hamilton D. C., Holmes N. C., Radousky H. B., Ree F. H., Mitchell A. C., Nicol M., 1988, *Science*, **240**, 779

Nettelmann N., Helled R., Fortney J. J., Redmer R., 2013, *Planet. Space Sci.*, **77**, 143

Pearl J. C., Conrath B. J., 1991, *Journal of Geophysical Research Supplement*, **96**, 18921

Pearl J. C., Conrath B. J., Hanel R. A., Pirraglia J. A., Coustenis A., 1990, *Icarus*, **84**, 12

Podolak M., Helled R., Schubert G., 2019, *MNRAS*, **487**, 2653

Ravasio A., et al., 2021, *Phys. Rev. Lett.*, **126**, 025003

Shah O., Alibert Y., Helled R., Mezger K., 2021, *A&A*, **646**, A162

Simon A. A., et al., 2020, *Space Sci. Rev.*, **216**, 17

Soderlund K. M., Stanley S., 2020, *Earth and Space Science Open Archive*, p. 17

Soderlund K. M., Heimpel M. H., King E. M., Aurnou J. M., 2013, *Icarus*, **224**, 97

Soubiran F., Militzer B., 2015, *The Astrophysical Journal*, **806**, 228

Soubiran F., Militzer B., 2016, *The Astrophysical Journal*, **829**, 14

Soyer D., Soubiran F., Helled R., 2020, *MNRAS*, **498**, 621

Soyer D., Zwick L., D’Orazio D. J., Saha P., 2021, *MNRAS*, **503**, L73

Stanley S., Bloxham J., 2004, *Nature*, **428**, 151

Stanley S., Bloxham J., 2006, *Icarus*, **184**, 556

Vazan A., Helled R., 2020, *A&A*, **633**, A50

Wicht J., Gastine T., Duarte L. D. V., Dietrich W., 2019, *A&A*, **629**, A125

This paper has been typeset from a $\text{\TeX}/\text{\LaTeX}$ file prepared by the author.